

# Waveform systematics for binary neutron star gravitational wave signals: Effects of spin, precession, and the observation of electromagnetic counterparts

Anuradha Samajdar and Tim Dietrich  
*Nikhef, Science Park, 1098 XG Amsterdam, The Netherlands*  
 (Dated: May 9, 2019)

Extracting the properties of a binary system emitting gravitational waves relies on models describing the last stages of the compact binary coalescence. In this article, we study potential biases inherent to current tidal waveform approximants for spinning and precessing systems. We perform a Bayesian study to estimate intrinsic parameters of highly spinning binary neutron star systems. Our analysis shows that one has to include the quadrupolar deformation of the neutron stars due to their rotation once dimensionless spins above  $\chi \sim 0.20$  are reached, otherwise the extracted intrinsic parameters are systematically biased. We find that at design sensitivity of Advanced LIGO and Virgo, it seems unlikely that for GW170817-like sources a clear imprint of precession will be visible in the analysis of the signal employing current waveform models. However, precession effects might be detectable for unequal mass configurations with spins larger than  $\chi > 0.2$ . We finalize our study by investigating possible benefits of a combined gravitational wave and electromagnetic detection. The presence of electromagnetic counterparts help in reducing the dimensionality of the parameter space with constraints on the sky location, source distance, and inclination. However, we note that although a small improvement in the estimation of the tidal deformability parameter is seen in these cases, changes in the intrinsic parameters are overall very small.

## I. INTRODUCTION

GW170817 marks a breakthrough in multi-messenger astronomy and is the first detected gravitational wave (GW) signal emerging from the coalescence of two neutron stars (NSs). This event allowed constraining the expansion rate of the universe [1], proved that NS mergers are the major cosmic source of r-process elements, e.g. [2–11], allowed a precise measurement of the speed difference between GWs and light [12], and placed constraints on alternative theories of gravity [13–15]. In addition, it supported the conjecture that NS mergers produce Gamma-Ray-Bursts (GRBs) [2, 16, 17] and enabled the scientific community to investigate the supranuclear equation of state (EOS) governing the interior of NSs. These constraints arise either purely from the analysis of the GW signal, e.g., Refs. [18–23], from a combination of GW and EM information, e.g. Refs. [24–28], or from a statistical analysis of a large set of possible EOSs, e.g., [29, 30].

To extract information from the detected GW signal, one needs to cross-correlate the data with model waveforms constructed from theoretical predictions. Within the framework of Bayesian analysis, this means that a multi-dimensional likelihood function has to be computed [31]. Because of the need to generate a large number of GW waveforms for evaluating the multidimensional likelihood integral numerous times, the computation of each individual waveform has to be sufficiently fast and, on the other hand, accurate enough for a precise measurement of the intrinsic source parameters.

Over the last years, there has been progress in modelling BNS coalescences by the development of improved analytical post-Newtonian (PN) based models, e.g. [32–36], state-of-the-art tidal effective-one-body (EOB) waveform approximants, e.g., [37–44] (and their

corresponding surrogates [45, 46]), or closed-form tidal models [47–50].

Bayesian studies characterizing the estimation of the tidal deformability and consequently the supranuclear EOS have been presented first in [51] with a PN based waveform model. This initial work has been extended and improved in a number of works (all based on PN approximants), e.g., Refs. [33, 52–54].

Relatively recently, Refs. [55, 56] investigated the importance of the inclusion of tidal effects for the extraction of the NS masses and spins using non-spinning hybrid tidal EOB – numerical relativity based injections, and the performance of different waveform approximants. Ref. [21] studied tidal EOB waveforms (including small effective spins parameters up to  $\chi_{\text{eff}} \approx 0.02$ ) and Ref. [57] investigated the imprint of the point-particle and tidal description for non-spinning BNS systems on parameter estimation (PE) results.

As per our knowledge, none of the existing works investigated the influence of large spins and precession for current state-of-the-art waveform approximants, or allowed a clear understanding of the effect of a confirmed EM counterpart, i.e., how different EM observations support the GW data analysis. To fill these gaps, we study equal and unequal mass BNS signals for a number of spin values and spin orientations, which enable a clear assessment of effects due to spin and precession. In addition, we analyse signals for which we restrict, according to different scenarios, the source location and/or inclination of the binary.

The article is structured as follows. In Sec. II we discuss briefly the numerical methods and employed waveform approximants. In Sec. III we investigate the effect of aligned spin and precession on the parameter estimation analyses. Sec. IV gives a short overview about the

effects of possible observed EM counterparts and their imprint on the GW data analysis. We summarize and conclude in Sec. V.

## II. METHODS

### A. Bayesian inference

In this article, we use a Bayesian approach for parameter estimation based on the `LALInference` module [31] available in the `LALSuite` package. In particular, we employ the Markov Chain Monte Carlo (MCMC) algorithm `lalinference_mcmc` [58]. Information about the parameters are encoded in the posterior probability distribution function

$$p(\vec{\theta}|\mathcal{H}_s, d) = \frac{p(\vec{\theta}|\mathcal{H}_s)p(d|\vec{\theta}, \mathcal{H}_s)}{p(d|\mathcal{H}_s)}, \quad (1)$$

where  $\vec{\theta}$  represents the parameter set and  $\mathcal{H}_s$  the hypothesis that a GW signal depending on the parameters  $\vec{\theta}$  is present in the data  $d$ . In addition to the parameter set common to a BBH signal  $\{m_1, m_2, \chi_1, \chi_2, \theta, \phi, \iota, \psi, D_L, t_c, \varphi_c\}$ , the two tidal deformability parameters  $\Lambda_A$  and  $\Lambda_B$  are present for a BNS system, see e.g. [57] for further details. The best measured quantity describing tidal effects is in fact a mass-weighted combination of the individual tidal deformabilities, e.g. [59],

$$\tilde{\Lambda} = \frac{16}{13} \sum_{i=1,2} \Lambda_i \frac{m_i^4}{M^4} \left(12 - 11 \frac{m_i}{M}\right). \quad (2)$$

The likelihood of obtaining a signal  $h(t)$  in data stream  $d(t)$ , which also includes the noise  $n(t)$ , is proportional to

$$p(d|\vec{\theta}, \mathcal{H}_s) \propto \exp \left[ -\frac{1}{2} (d - h|d - h) \right]. \quad (3)$$

### B. Waveform models

A frequency-domain gravitational waveform is given by

$$\tilde{h}(f) = \tilde{A}(f) e^{-i\Psi(f)}, \quad (4)$$

where the phase  $\Psi(f)$  can be approximated as a sum of the non-spinning point-particle (PP) contribution, a spin-orbit (SO) contribution, a spin-spin (SS) contribution, and tidal contribution (Tides):

$$\Psi(f) = \Psi_{\text{PP}}(f) + \Psi_{\text{SO}}(f) + \Psi_{\text{SS}}(f) + \Psi_{\text{Tides}}(f). \quad (5)$$

The PE analyses of the BNS signal GW170817 in [21–23] have also been done with BNS waveform models where the tidal phasing given by the `NRTidal` framework [47] is added to the BBH inspiral-merger-ringdown

Name	$m_1$	$m_2$	$M_{\text{total}}$	q	$\Lambda_1$	$\Lambda_2$	$\tilde{\Lambda}$
Eq	1.375	1.375	2.75	1.00	292	292	292
Un	1.68	1.13	2.81	0.67	77	973	303

TABLE I. Overview of the intrinsic parameters of the injected sources, the individual spins are varied in addition. The columns refer to the individual masses, the total mass, the mass ratio, the individual tidal deformabilities, and the effective tidal deformability  $\tilde{\Lambda}$ .

waveform models `IMRPhenomD` [60], `IMRPhenomPv2` [61], and `SEOBNRv4_ROM` [62, 63]. Details of construction of these BNS waveform models from their BBH counterparts are presented in [49].

In this article, we restrict the analysis to three waveform models:

- (i) The spin-aligned `IMRPhenomD_NRTidal` (henceforth `IMRDNRT`) model as discussed in [49]. This model does not include EOS-dependent quadrupole-monopole terms, i.e., all spin-spin contributions are treated similar to that of a binary black hole system.
- (ii) The precessing `IMRPhenomPv2_NRTidal` (henceforth `IMRPNRT`) model as discussed in [49]. This model includes the EOS-dependent quadrupole-monopole term up to the 3PN order.
- (iii) The spin-aligned `IMRPhenomD_NRTidal` for which we add the EOS dependence to the spin-spin interactions (henceforth `IMRDNRT_Q`) up to the 3PN order.

The main spin contribution is characterized by the aligned-spin effective parameter

$$\chi_{\text{eff}} = \frac{m_1 \chi_{1\parallel} + m_2 \chi_{2\parallel}}{m_1 + m_2}, \quad (6)$$

where  $\chi_{i\parallel} = \frac{\vec{S}_i}{m_i^2} \cdot \hat{L}$  is the dimensionless spin parameter aligned with the direction of the orbital angular momentum  $\hat{L}$ . Precession effects in `IMRPNRT` are in addition characterized by the single-spin parameter [64]

$$\chi_p = \max \left( \chi_{1\perp}, \frac{3 + 4q}{4 + 3q} q \chi_{2\perp} \right), \quad (7)$$

where  $\chi_{1\perp}$  and  $\chi_{2\perp}$  denote the spin components perpendicular to the orbital angular momentum and  $q$  is the mass-ratio defined below in Sec. II C. We have investigated effects of varying  $\Psi_{\text{PP}}(f)$  and  $\Psi_{\text{Tides}}(f)$  in Ref. [57]. Here, we focus on the effects of  $\Psi_{\text{SO}}(f)$ ,  $\Psi_{\text{SS}}(f)$ , precession, as well as possible improvements in the PE analyses due to a more constrained parameter space from accompanying EM counterparts.

### C. Injection study

As an EOS which is in agreement with current constraints [21], we choose the component masses and tidal

deformabilities following the APR4 EOS [65]. We place the sources at a luminosity distance of  $D_L = 50$  Mpc. The intrinsic parameters of the two employed BNS sources are summarized in Tab. I. We choose values of the dimensionless spin parameter varying from 0.05 to 0.50. We simulate spinning BNS sources and investigate biases in estimation of the binary parameters in presence of three different spin configurations

- (i) spins aligned with the direction of the orbital angular momentum (aligned spins) – denoted as  $(\uparrow\uparrow)$ ;
- (ii) spins lying in the orbital plane (in-plane spins) – denoted as  $(\leftarrow \rightarrow)$ ;
- (iii) spins oriented at an angle of  $45^\circ$  with the direction of the orbital angular momentum (misaligned spins) – denoted as  $(\nearrow \searrow)$ .

Our simulations are done using the waveform model IMRPNRT and are analyzed with IMRDNRT, IMRPNRT, and IMRDNRT<sub>Q</sub>. All simulations are done in simulated, Gaussian noise using noise power spectral density of the design sensitivity of Advanced LIGO and Virgo’s detector network [66]. We note that our simulations are quite loud with matched filter signal to noise ratios of 80-90, so our results are dominated mainly by systematics rather than statistical uncertainties.

Our priors are motivated by the study of GW170817, Ref. [21]. Consequently, the recovery is done with a uniform prior on the component tidal deformabilities  $\Lambda_1$  and  $\Lambda_2$  between 0 and 5000. Priors on dimensionless spin magnitudes are distributed uniformly between 0 and 0.7. The chirp mass  $\mathcal{M} = (m_1 m_2)^{3/5} / M^{1/5}$ , is sampled uniformly between 1.184 and 2.168 with mass-ratio  $q = m_2 / m_1$  restricted between 0.125 and 1. Priors on the other parameters are given explicitly in the following sections according to the individual analysis performed.

### III. EXTRACTING INTRINSIC PARAMETERS IN PRESENCE OF SPINS

In this section, we simulate equal-mass and unequal-mass sources by varying their dimensionless spin magnitudes. Apart from their spins, the intrinsic parameters of each of the equal and unequal mass source are kept fixed and are listed in Tab. I.

In addition to the priors mentioned above (Sec. II C), we sample the distance uniformly in a co-moving volume up to 100Mpc. The priors on the sky position as well as the inclination of the binary are uniformly distributed on the sphere.

#### A. Effects of aligned spins

For each of the sources in Tab. I, we vary the dimensionless spin magnitudes on each component mass

from 0.05 to 0.5 in steps of 0.05. Henceforth, we refer to an aligned-spin equal-mass system with effective spin parameter  $\chi_{\text{eff}}$  as  $\text{Eq}_{\chi_{\text{eff}}}^{\uparrow\uparrow}$ . Similarly, the unequal-mass aligned-spinning systems are denoted by  $\text{Un}_{\chi_{\text{eff}}}^{\uparrow\uparrow}$ .

#### Equal-mass binaries:

In Fig. 1, we show the posterior probability distribution functions (PDFs) of the intrinsic parameters for each of the injected spin values for the equal-mass setup. Considering the extraction of intrinsic binary properties from the equal-mass binary, we find generally that with IMRPNRT or IMRDNRT<sub>Q</sub> the binary parameters are better recovered than for the corresponding IMRDNRT setup. This points to the importance of the spin-spin interactions, in particular for spins  $\chi > 0.2$ .

Independent of the model, for an increasing spin magnitude, the extraction of the total mass, mass ratio, and tidal deformability becomes less restrictive. This is most visible for IMRPNRT when considering the tidal deformability parameter  $\tilde{\Lambda}$ . Although the injected value (horizontal gray lines for each panel in Fig. 1) lies almost always within the 90% credible interval (given by the colored horizontal lines; the colors corresponding to each waveform approximant), the posterior distribution becomes increasingly broad for larger spins. In comparison, the IMRDNRT<sub>Q</sub> model restricts the tidal deformability better than IMRPNRT. A similar effect was discussed in Ref. [57] for non-spinning injections, where it was pointed that the reduction of the parameter space helps to improve the extraction of individual parameters. Trivially, this observation can be generalized to aligned-spin configurations.

With all other parameters being kept fixed, a larger value of  $\chi_{\text{eff}}$  causes a longer inspiral phase [67–69]. It has been shown [70] that effects of larger spin may be compensated by changing values of the mass ratio [71] or even total mass. We do see a similar trend in the recovered mass ratios as they become smaller for larger spin magnitudes. For these cases, the estimated total masses are higher, which leads to a recovered chirp mass closer to the injected value.

Among the best recovered parameters for all models is the effective aligned-spin parameter  $\chi_{\text{eff}}$ . This can be understood by the fact that the effective spin is mainly determined from the long early-inspiral containing several thousand GW cycles, since the leading order spin-orbit contribution enters already at the 1.5PN order<sup>1</sup>. Only the IMRDNRT approximant shows noticeable differences with respect to the injected values, which again emphasizes the importance of incorporation of the spin-induced quadrupole-monopole term.

It is encouraging that standard waveform approximants are able to determine spin values of  $\sim 0.05$

<sup>1</sup> We note that although the mass ratio enters at even earlier PN order, it is measured better at higher frequencies, which follows e.g. from Fig. 2 of [72] and is in agreement with our results

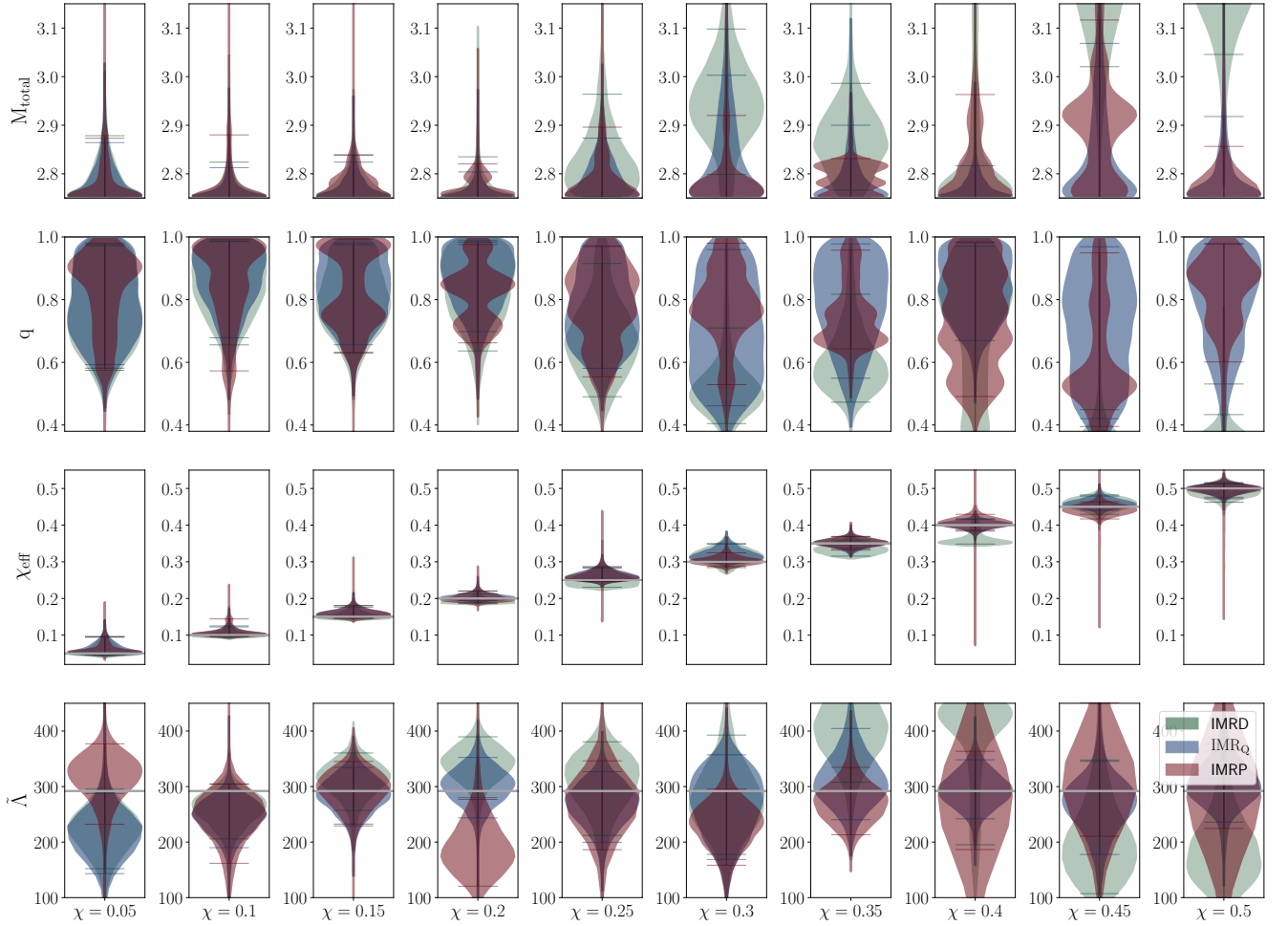


FIG. 1. Equal mass configuration  $\text{Eq}_{\chi_{\text{eff}}}^{\uparrow\uparrow}$ . The extracted posteriors are marked green for the IMRDNRT approximant, red for IMRPNRT, and blue for IMRDNRT<sub>Q</sub>. Injected value are marked with a horizontal gray line and 90% confidence intervals are shown with green, red, and blue horizontal lines for the individual approximants.

once the design sensitivity of advanced GW detectors is reached. This shows that there is the chance of detecting millisecond pulsars via GW astronomy.

In general, it seems possible to reliably estimate intrinsic parameters up to an aligned spin of  $\chi_{\text{eff}} \sim 0.4$  once the spin-spin interactions include EOS dependence as in IMRDNRT<sub>Q</sub> and IMRPNRT. We note that this value is well above the largest dimensionless spin observed in a BNS system to date ( $\chi \sim 0.05$  for PSR J1946+2052 [73]), and therefore is also above the low-spin prior of  $\chi < 0.05$  employed in some of the LVC analyses, e.g. [21–23]. It is also larger than the dimensionless spin of PSR J1807–2500B which is, with a rotation frequency of 239Hz [74, 75], currently the fastest spinning NS in a binary system.

### Unequal-mass binaries:

In Fig. 2, we show the posterior probability distribution functions (PDFs) of the intrinsic parameters for each of the injected spin values for the unequal-mass

setup. The results for the unequal-mass configurations are in line with our equal-mass studies. We find that IMRPNRT and IMRDNRT<sub>Q</sub> approximants perform best and that above a spin value of  $\chi \sim 0.25$  the quadrupolar deformation of the NSs due to its own spin becomes important. Thus, systematic biases are introduced in the IMRDNRT model in which the EOS-dependent quadrupolar deformation is not included. These biases result in a larger estimated total mass and smaller mass ratio (as for the equal-mass case).

Considering the effective spin  $\chi_{\text{eff}}$ , we find that as for the equal mass case the injected value (denoted by horizontal gray lines in each panel in Fig. 2) is recovered robustly and always remains within the 90% credible interval (colored horizontal lines, with the colors corresponding to each waveform approximant). The injected value of  $\tilde{\Lambda}$  is always contained within the posterior distribution of the  $\tilde{\Lambda}$  parameter for all waveform approximants. As for the equal-mass case, the posterior distribution functions with IMRPNRT recovery broaden with gradual in-

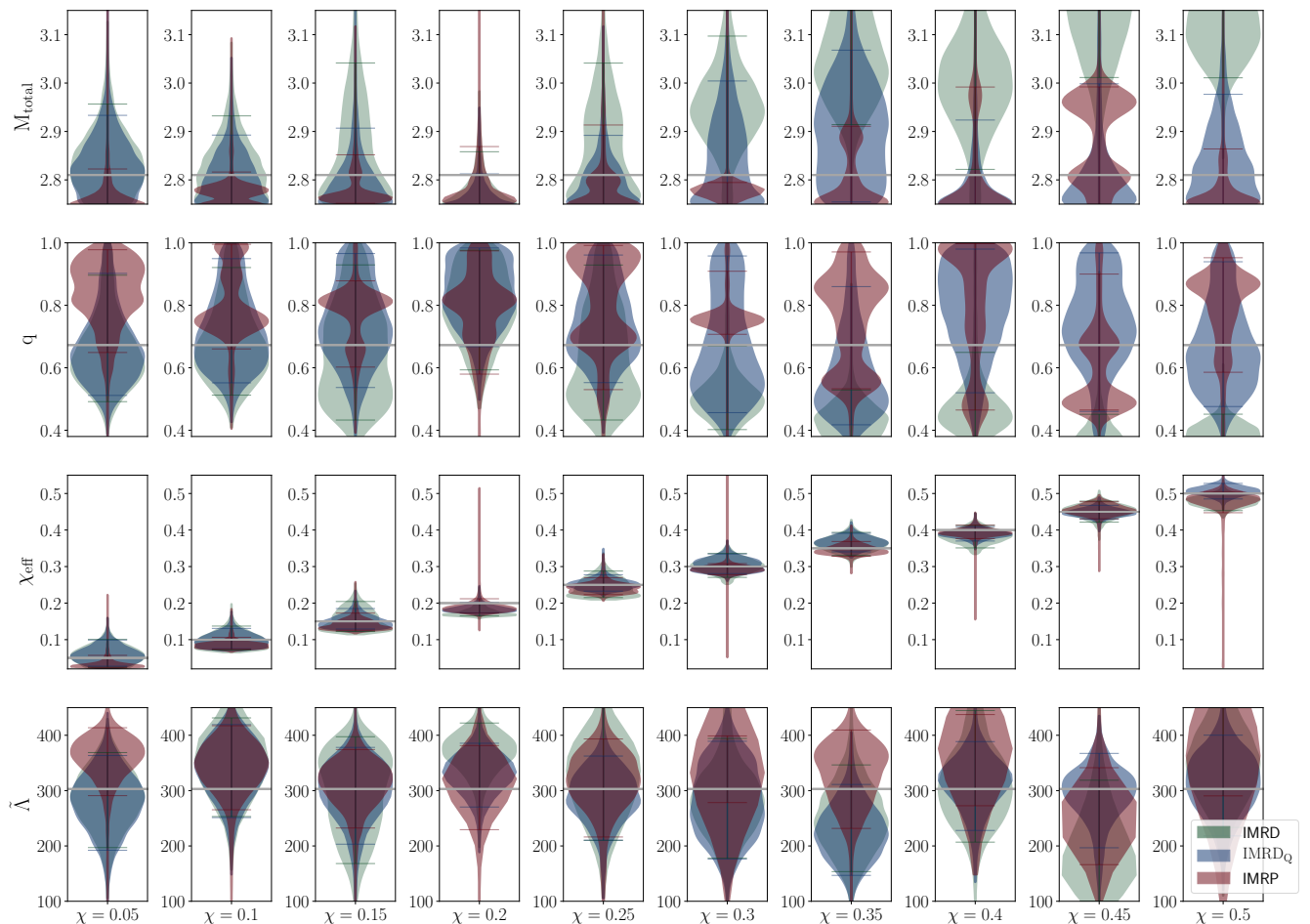


FIG. 2. As Fig. 1 but for the unequal-mass configurations  $Un_{\chi_{\text{eff}}}^{\uparrow\uparrow}$ .

crease in spins. However, the same does not hold true for IMRDNRT<sub>Q</sub> recovery.

### B. Effects of precessing spins

We now consider systems with precession, i.e., setups for which a non-vanishing spin component inside the orbital plane exists. To reduce computational costs, we study only setups for the spin values  $\chi = 0.05, 0.2, 0.4$  and discard other spin values studied for the aligned cases.

**Equal-mass binaries:** The results from the precessing spin equal-mass simulations are shown in Fig. 3. We show in the left panel results for the in-plane configuration and in the right panel results for the misaligned setup.

For the in-plane configuration, the simulated values of total mass  $M$  and mass ratio  $q$  lie within the 90% upper bound values of their posterior distributions. The effective spin  $\chi_{\text{eff}}$  is also recovered within the 90% confidence region for in-plane systems although the confidence interval is quite broad to be able to make conclusive statements. For all values of spin magnitudes, recovery

with the IMRPNRT model includes the injected value of the precessing spin parameter  $\chi_P$  within the 90% confidence interval of the posterior distribution. However, the confidence intervals are generally too large to claim confidently a measurement of precession effects. When the injected spin magnitude is large ( $\chi \sim 0.4$ ), we note that IMRDNRT performs poorly to recover the extracted tidal deformability whereas IMRDNRT<sub>Q</sub> and IMRPNRT perform similarly, in spite of IMRDNRT<sub>Q</sub> being an aligned spinning model.

In an improved model of the NRTidal framework [76], higher order spin-squared and spin-cubed terms are added, along with their respective spin-induced moments. This might improve the estimation of the tidal deformability in the case of large spins.

For the misaligned configurations (right panel of Fig. 3), the total mass  $M$  is recovered well with IMRDNRT, but for large spins we find similar biases as for the aligned configuration for IMRDNRT. The  $\chi_{\text{eff}}$  parameter however, seems to be quite robustly measured. We find the tidal deformability to be loosely constrained with IMRPNRT for this spin orientation.

Overall, our observations might hint towards the fact

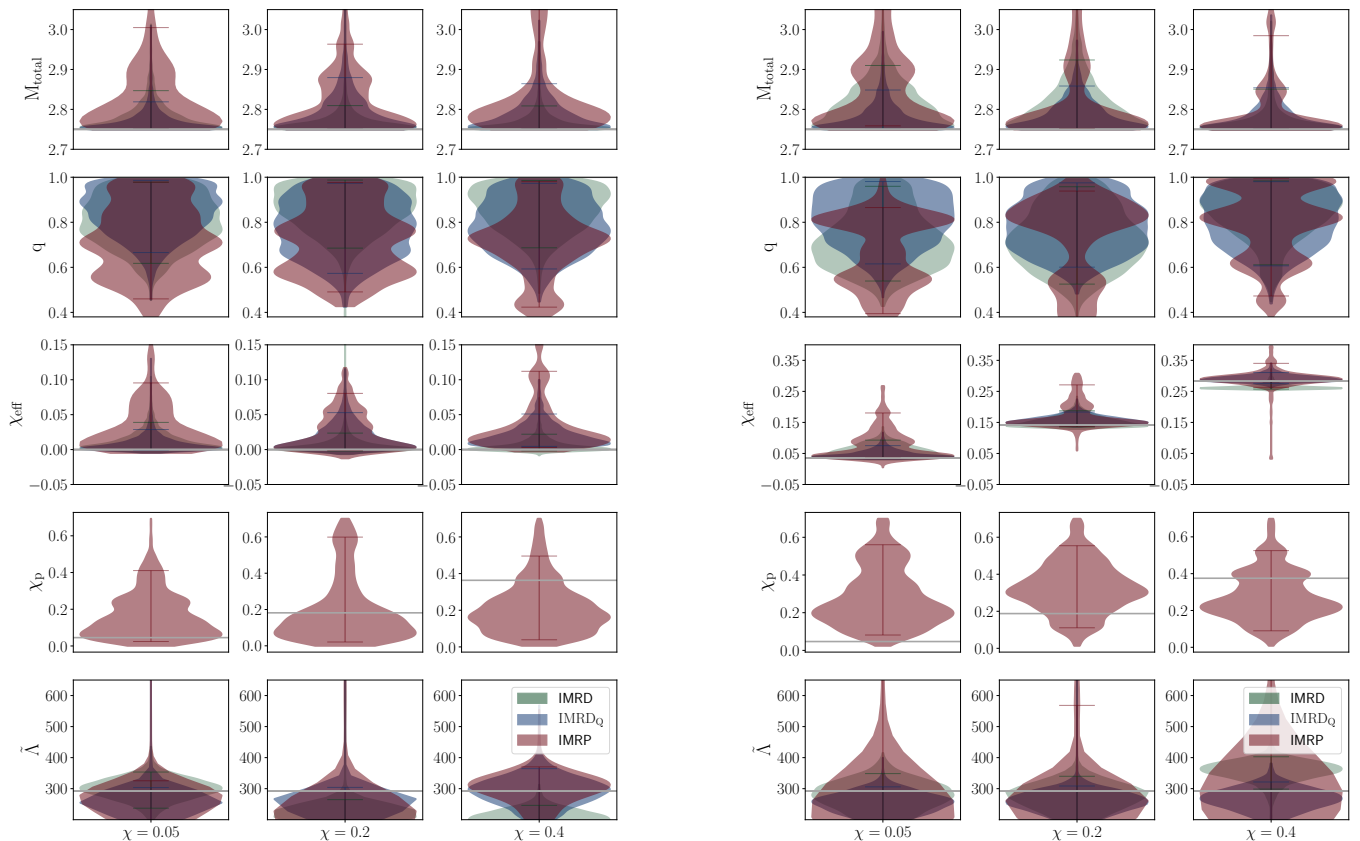


FIG. 3. Equal mass system  $E_{q_x}$  with in in-plane spin ( $\longleftrightarrow$ ) (left) and with mis-aligned spin ( $\nwarrow \nearrow$ ) (right). Injected values are marked with a horizontal gray line and 90% confidence intervals are shown with red/green horizontal lines.

that a further improvement of the precession dynamics is needed. A possible extension of the IMRPNRT model with a two-spin precession description as in [77] might help to further improve our capability to extract precession effects from future events. On the other hand, while computationally more expensive, one could also extend the precessing EOB model [78] with the NRTidal framework to allow a better modelling of the inspiral of precessing BNSs.

**Unequal-mass binaries:** The results from the simulations of the unequal-mass setup for in-plane (left panel) and misaligned spin (right panel) are shown in Fig. 4. All waveform models include the injected parameters within the 90% confidence intervals of the posterior distributions, although it appears again that  $\chi_{\text{eff}}$  is slightly over-estimated for the  $\chi = 0.05$  configuration. While most observations made for the equal-mass sources hold also for the unequal-mass sources, we find that for very large misaligned spins ( $\chi = 0.4$  and the  $\nwarrow \nearrow$  case) the IMRPNRT posterior of  $\chi_p$  excludes non-precessing setups. This shows that, as expected, precession effects are easier to detect for unequal mass setups than for equal mass systems.

#### IV. INCORPORATING INFORMATION FROM ELECTROMAGNETIC COUNTERPARTS

In addition to the study of spin effects, presented in the previous section, we want to understand the possible interplay between GW astronomy and EM observations. For this purpose, we will employ the configurations  $Un_\chi^{(\uparrow\uparrow)}$ ,  $Un_\chi^{(\longleftrightarrow)}$ ,  $Un_\chi^{(\nwarrow \nearrow)}$  with  $\chi = 0.2$  and  $0.4$ , i.e., a total of six different physical setups. To save further computational costs, we restrict our analysis to the IMRPNRT model since it is the only precessing model and analyse for the observational scenarios II and III (kilonova and GRB respectively, cf. Tab. II) only the  $\chi = 0.2$  case and with an aligned-spinning configuration.

GW170817 [12] has shown the huge variety of EM signals which can be detected in coincidence or as a follow-up of a potential GW trigger. We consider here four different scenarios:

**I. the absence of an EM counterpart:** For such scenarios one keeps the GW standard priors on the distance and sky location.

**II. a kilonova detection:** In cases where a kilonova

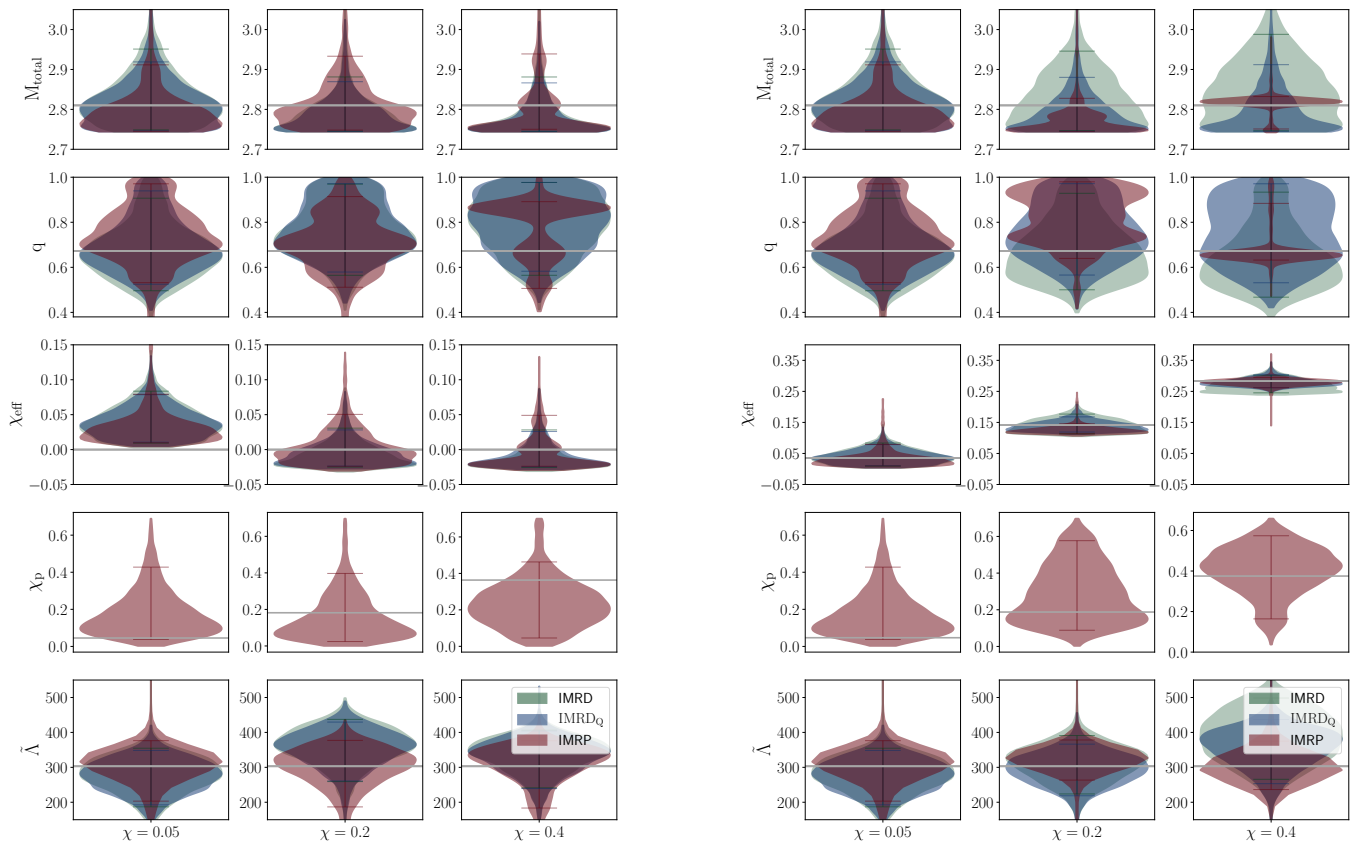


FIG. 4. Unequal mass system  $Un_x$  with in in-plane spin ( $\leftrightarrow$ ) (left) and with mis-aligned spin ( $\nwarrow \nearrow$ ) (right). Injected values are marked with a horizontal gray line and 90% confidence intervals are shown with red/green horizontal lines.

gets detected, the good angular resolution of optical or near-optical telescopes fixes the sky location and provides, due to the redshift measurement of the host galaxy, a constraint on the source distance.

**III. a GRB detection:** The observation of a GRB generally provides broad information about the sky location. Furthermore, since GRBs are beamed within a small angle, they also provide additional estimates of the inclination of the binary with respect to the line of sight, e.g., [2, 79–83].

**IV. kilonova and GRB detection:** As for GW170817 it can be expected that for a number of BNS mergers, one detects both a kilonova and a GRB which combines the constraints of (ii) and (iii).

We provide for all four cases the priors for the distance, sky localization ( $\theta, \phi$ ), and inclination of the system  $\iota$  in Tab. II.

For the interpretation of the imprint of the combined EM and GW analyses, we compute the systematic bias

Counterpart	Priors			
	$D_L$ [Mpc]	$\theta$ [deg.]	$\phi$ [deg.]	$\iota$ [deg.]
Injected values	50	60	60	25
No EM counterpart	[1,100]	[0,180]	[-90,90]	[0, 180]
Kilonova	[45,55]	fixed	fixed	[0, 180]
GRB	[1,100]	[35,85]	[35,85]	[0, 50]
Kilonova + GRB	[45,55]	fixed	fixed	[0, 50]

TABLE II. Overview about the prior choices for different observational scenarios considering absence of an EM counterpart, a detection of a kilonova, a detection of a GRB, and the combined detection of a kilonova and a GRB.

with the standard accuracy statistic (stacc) defined as

$$S = \sqrt{\frac{1}{N} \sum_{i=1}^N (x_i - x_{\text{inj}})^2}, \quad (8)$$

where  $N$  is the number of samples,  $x_i$  is the  $i^{\text{th}}$  posterior sample and  $x_{\text{inj}}$  is the injected value of the parameter  $x$ .

We find that although the covered parameter space is reduced due to the additional EM information, there are only minor changes in the recovered estimates and the incorporation of the source distance, location, and inclination does not noticeably improve the GW data analysis.







- [8] N. R. Tanvir *et al.*, *Astrophys. J.* **848**, L27 (2017), arXiv:1710.05455 [astro-ph.HE].
- [9] S. Rosswog, J. Sollerman, U. Feindt, A. Goobar, O. Korobkin, R. Wollaeger, C. Fremling, and M. M. Kasliwal, *Astron. Astrophys.* **615**, A132 (2018), arXiv:1710.05445 [astro-ph.HE].
- [10] B. P. Abbott *et al.* (LIGO Scientific, Virgo), *Astrophys. J.* **850**, L39 (2017), arXiv:1710.05836 [astro-ph.HE].
- [11] S. Ascenzi *et al.*, (2018), arXiv:1811.05506 [astro-ph.HE].
- [12] *Astrophys. J.* **848**, L12 (2017), arXiv:1710.05833 [astro-ph.HE].
- [13] J. M. Ezquiaga and M. Zumalacárregui, *Phys. Rev. Lett.* **119**, 251304 (2017), arXiv:1710.05901 [astro-ph.CO].
- [14] T. Baker, E. Bellini, P. G. Ferreira, M. Lagos, J. Noller, and I. Sawicki, *Phys. Rev. Lett.* **119**, 251301 (2017), arXiv:1710.06394 [astro-ph.CO].
- [15] P. Creminelli and F. Vernizzi, *Phys. Rev. Lett.* **119**, 251302 (2017), arXiv:1710.05877 [astro-ph.CO].
- [16] B. Paczynski, *Astrophys. J.* **308**, L43 (1986).
- [17] B. P. Abbott *et al.* (LIGO Scientific, Virgo, Fermi-GBM, INTEGRAL), *Astrophys. J.* **848**, L13 (2017), arXiv:1710.05834 [astro-ph.HE].
- [18] B. P. Abbott *et al.* (Virgo, LIGO Scientific), *Phys. Rev. Lett.* **119**, 161101 (2017), arXiv:1710.05832 [gr-qc].
- [19] L. Dai, T. Venumadhav, and B. Zackay, (2018), arXiv:1806.08793 [gr-qc].
- [20] S. De, D. Finstad, J. M. Lattimer, D. A. Brown, E. Berger, and C. M. Biwer, (2018), arXiv:1804.08583 [astro-ph.HE].
- [21] B. P. Abbott *et al.* (Virgo, LIGO Scientific), (2018), arXiv:1805.11579 [gr-qc].
- [22] B. P. Abbott *et al.* (Virgo, LIGO Scientific), (2018), arXiv:1805.11581 [gr-qc].
- [23] B. P. Abbott *et al.* (LIGO Scientific, Virgo), (2018), arXiv:1811.12907 [astro-ph.HE].
- [24] D. Radice, A. Perego, F. Zappa, and S. Bernuzzi, *Astrophys. J.* **852**, L29 (2018), arXiv:1711.03647 [astro-ph.HE].
- [25] A. Bauswein, O. Just, H.-T. Janka, and N. Stergioulas, *Astrophys. J.* **850**, L34 (2017), arXiv:1710.06843 [astro-ph.HE].
- [26] M. W. Coughlin *et al.*, (2018), arXiv:1805.09371 [astro-ph.HE].
- [27] D. Radice and L. Dai, (2018), arXiv:1810.12917 [astro-ph.HE].
- [28] M. W. Coughlin, T. Dietrich, B. Margalit, and B. D. Metzger, (2018), arXiv:1812.04803 [astro-ph.HE].
- [29] E. Annala, T. Gorda, A. Kurkela, and A. Vuorinen, *Phys. Rev. Lett.* **120**, 172703 (2018), arXiv:1711.02644 [astro-ph.HE].
- [30] E. R. Most, L. R. Weih, L. Rezzolla, and J. Schaffner-Bielich, (2018), arXiv:1803.00549 [gr-qc].
- [31] J. Veitch *et al.*, *Phys. Rev.* **D91**, 042003 (2015), arXiv:1409.7215 [gr-qc].
- [32] T. Damour, A. Nagar, and L. Villain, *Phys. Rev.* **D85**, 123007 (2012), arXiv:1203.4352 [gr-qc].
- [33] M. Agathos, J. Meidam, W. Del Pozzo, T. G. F. Li, M. Tompitak, J. Veitch, S. Vitale, and C. Van Den Broeck, *Phys. Rev.* **D92**, 023012 (2015), arXiv:1503.05405 [gr-qc].
- [34] X. Jiménez Forteza, T. Abdelsalhin, P. Pani, and L. Gualtieri, *Phys. Rev.* **D98**, 124014 (2018), arXiv:1807.08016 [gr-qc].
- [35] T. Abdelsalhin, L. Gualtieri, and P. Pani, *Phys. Rev.* **D98**, 104046 (2018), arXiv:1805.01487 [gr-qc].
- [36] P. Pani, L. Gualtieri, T. Abdelsalhin, and X. Jiménez Forteza, (2018), arXiv:1810.01094 [gr-qc].
- [37] S. Bernuzzi, A. Nagar, T. Dietrich, and T. Damour, *Phys. Rev. Lett.* **114**, 161103 (2015), arXiv:1412.4553 [gr-qc].
- [38] K. Hotokezaka, K. Kyutoku, Y.-i. Sekiguchi, and M. Shibata, *Phys. Rev.* **D93**, 064082 (2016), arXiv:1603.01286 [gr-qc].
- [39] T. Hinderer *et al.*, *Phys. Rev. Lett.* **116**, 181101 (2016), arXiv:1602.00599 [gr-qc].
- [40] J. Steinhoff, T. Hinderer, A. Buonanno, and A. Taracchini, *Phys. Rev.* **D94**, 104028 (2016), arXiv:1608.01907 [gr-qc].
- [41] T. Dietrich and T. Hinderer, *Phys. Rev.* **D95**, 124006 (2017), arXiv:1702.02053 [gr-qc].
- [42] A. Nagar *et al.*, (2018), arXiv:1806.01772 [gr-qc].
- [43] A. Nagar, F. Messina, P. Rettengo, D. Bini, T. Damour, A. Geralico, S. Akcay, and S. Bernuzzi, (2018), arXiv:1812.07923 [gr-qc].
- [44] S. Akcay, S. Bernuzzi, F. Messina, A. Nagar, N. Ortiz, and P. Rettengo, (2018), arXiv:1812.02744 [gr-qc].
- [45] B. D. Lackey, S. Bernuzzi, C. R. Galley, J. Meidam, and C. Van Den Broeck, *Phys. Rev.* **D95**, 104036 (2017), arXiv:1610.04742 [gr-qc].
- [46] B. D. Lackey, M. Pürrer, A. Taracchini, and S. Marsat, (2018), arXiv:1812.08643 [gr-qc].
- [47] T. Dietrich, S. Bernuzzi, and W. Tichy, *Phys. Rev. D* **96**, 121501 (2017).
- [48] T. Dietrich, S. Bernuzzi, B. Bruegmann, and W. Tichy (2018) arXiv:1803.07965 [gr-qc].
- [49] T. Dietrich *et al.*, (2018), arXiv:1804.02235 [gr-qc].
- [50] K. Kawaguchi, K. Kiuchi, K. Kyutoku, Y. Sekiguchi, M. Shibata, and K. Taniguchi, (2018), arXiv:1802.06518 [gr-qc].
- [51] W. Del Pozzo, T. G. F. Li, M. Agathos, C. Van Den Broeck, and S. Vitale, *Phys. Rev. Lett.* **111**, 071101 (2013), arXiv:1307.8338 [gr-qc].
- [52] B. D. Lackey and L. Wade, *Phys. Rev.* **D91**, 043002 (2015), arXiv:1410.8866 [gr-qc].
- [53] M. Favata, *Phys. Rev. Lett.* **112**, 101101 (2014), arXiv:1310.8288 [gr-qc].
- [54] L. Wade, J. D. E. Creighton, E. Ochsner, B. D. Lackey, B. F. Farr, T. B. Littenberg, and V. Raymond, *Phys. Rev.* **D89**, 103012 (2014), arXiv:1402.5156 [gr-qc].
- [55] R. Dudi, F. Pannarale, T. Dietrich, M. Hannam, S. Bernuzzi, F. Ohme, and B. Bruegmann, (2018), arXiv:1808.09749 [gr-qc].
- [56] F. Messina, R. Dudi, A. Nagar, and S. Bernuzzi, (2019), arXiv:1904.09558 [gr-qc].
- [57] A. Samajdar and T. Dietrich, (2018), arXiv:1810.03936 [gr-qc].
- [58] C. L. Rodriguez, B. Farr, V. Raymond, W. M. Farr, T. B. Littenberg, D. Fazi, and V. Kalogera, *Astrophys. J.* **784**, 119 (2014), arXiv:1309.3273 [astro-ph.HE].
- [59] E. E. Flanagan and T. Hinderer, *Phys. Rev.* **D77**, 021502 (2008), arXiv:0709.1915 [astro-ph].
- [60] S. Khan, S. Husa, M. Hannam, F. Ohme, M. Pürrer, X. Jiménez Forteza, and A. Bohé, *Phys. Rev.* **D93**, 044007 (2016), arXiv:1508.07253 [gr-qc].
- [61] P. Schmidt, F. Ohme, and M. Hannam, *Phys. Rev.* **D91**, 024043 (2015), arXiv:1408.1810 [gr-qc].
- [62] A. Bohe *et al.*, *Phys. Rev.* **D95**, 044028 (2017), arXiv:1611.03703 [gr-qc].

- [63] M. Pürrer, *Class. Quant. Grav.* **31**, 195010 (2014), arXiv:1402.4146 [gr-qc].
- [64] P. Schmidt, M. Hannam, and S. Husa, *Phys. Rev.* **D86**, 104063 (2012), arXiv:1207.3088 [gr-qc].
- [65] J. S. Read, B. D. Lackey, B. J. Owen, and J. L. Friedman, *Phys. Rev.* **D79**, 124032 (2009), arXiv:0812.2163 [astro-ph].
- [66] “<https://dcc.ligo.org/ligo-t1500293/public>,” .
- [67] M. Campanelli, C. O. Lousto, and Y. Zlochower, *Phys. Rev.* **D74**, 041501 (2006), arXiv:gr-qc/0604012 [gr-qc].
- [68] S. Bernuzzi, T. Dietrich, W. Tichy, and B. Brügmann, *Phys. Rev.* **D89**, 104021 (2014), arXiv:1311.4443 [gr-qc].
- [69] T. Dietrich, S. Bernuzzi, M. Ujevic, and W. Tichy, *Phys. Rev.* **D95**, 044045 (2017), arXiv:1611.07367 [gr-qc].
- [70] F. Ohme, *Bridging the gap between post-Newtonian theory and numerical relativity in gravitational-wave data analysis*, doctoralthesis, Universität Potsdam (2012).
- [71] E. Baird, S. Fairhurst, M. Hannam, and P. Murphy, *Phys. Rev.* **D87**, 024035 (2013), arXiv:1211.0546 [gr-qc].
- [72] I. Harry and T. Hinderer, *Class. Quant. Grav.* **35**, 145010 (2018), arXiv:1801.09972 [gr-qc].
- [73] K. Stovall *et al.*, *Astrophys. J.* **854**, L22 (2018), arXiv:1802.01707 [astro-ph.HE].
- [74] D. R. Lorimer, *Living Rev. Rel.* **11**, 8 (2008), arXiv:0811.0762 [astro-ph].
- [75] J. M. Lattimer, *Ann. Rev. Nucl. Part. Sci.* **62**, 485 (2012), arXiv:1305.3510 [nucl-th].
- [76] T. Dietrich *et al.*, in prep..
- [77] S. Khan, K. Chatziioannou, M. Hannam, and F. Ohme, (2018), arXiv:1809.10113 [gr-qc].
- [78] Y. Pan, A. Buonanno, A. Taracchini, L. E. Kidder, A. H. Mroué, H. P. Pfeiffer, M. A. Scheel, and B. Szilágyi, *Phys. Rev.* **D89**, 084006 (2014), arXiv:1307.6232 [gr-qc].
- [79] B. Paczynski, *Acta Astron.* **41**, 257 (1991).
- [80] R. Narayan, B. Paczynski, and T. Piran, *Astrophys. J.* **395**, L83 (1992), arXiv:astro-ph/9204001 [astro-ph].
- [81] A. Nathanail, *Galaxies* **6**, 119 (2018), arXiv:1808.05794 [astro-ph.HE].
- [82] E. T. H. van Eerten, G. Ryan, R. Ricci, J. M. Burgess, M. Wieringa, L. Piro, S. B. Cenko, and T. Sakamoto, (2018), arXiv:1808.06617 [astro-ph.HE].
- [83] Y. Wu and A. MacFadyen, *Astrophys. J.* **869**, 55 (2018), arXiv:1809.06843 [astro-ph.HE].